Sound velocities of compressed Fe₃C from simultaneous synchrotron X-ray diffraction and nuclear resonant scattering measurements

Lili Gao,[a,b]* Bin Chen,[a] Michael Lerche,[b,c] Esen E. Alp,[b] Wolfgang Sturhahn,[b] Jiyong Zhao,[b] Hasan Yavaş[a,b] and Jie Li[a]

[a]Department of Geology, University of Illinois, Urbana, IL 60801, USA, [b]Advanced Photon Source, Argonne National Laboratory, Argonne, IL 60439, USA, and [c]High Pressure Synergetic Consortium, Carnegie Institution of Washington, Argonne, IL 60439, USA. E-mail: liligao2@illinois.edu

The applications of nuclear resonant scattering in laser-heated diamond anvil cells have provided an important probe for the magnetic and vibrational properties of ^{57}Fe-bearing materials under high pressure and high temperature. Synchrotron X-ray diffraction is one of the most powerful tools for studying phase stability and equation of state over a wide range of pressure and temperature conditions. Recently an experimental capability has been developed for simultaneous nuclear resonant scattering and X-ray diffraction measurements using synchrotron radiation. Here the application of this method to determine the sound velocities of compressed Fe₃C is shown. The X-ray diffraction measurements allow detection of microscale impurities, phase transitions and chemical reactions upon compression or heating. They also provide information on sample pressure, grain size distribution and unit cell volume. By combining the Debye velocity extracted from the nuclear resonant inelastic X-ray scattering measurements and the structure, density and elasticity data from the X-ray diffraction measurements simultaneously obtained, more accurate sound velocity data can be derived. Our results on few-crystal and powder samples indicate strong anisotropy in the sound velocities of Fe₃C under ambient conditions.

Keywords: phonon density of state; anisotropy; impurity; Debye; APS.

1. Introduction

Nuclear resonant scattering (NRS) methods, including synchrotron Mössbauer spectroscopy (SMS) and nuclear resonant inelastic X-ray scattering (NRIXS), utilize synchrotron radiation with meV energy resolution to probe the magnetic structures and vibrational properties of resonant isotopes (Sturhahn, 2004). A commonly used resonant isotope is ^{57}Fe. Combined with diamond anvil cells (DACs) and laser heating techniques, NRIXS and SMS have been widely used to probe the elastic, thermodynamic and magnetic properties of iron-bearing materials under high pressures (e.g. Mao et al., 2001, 2004; Lin et al., 2003a, 2004; Sturhahn & Jackson, 2007; Gao et al., 2008) and at high temperatures (Shen et al., 2004; Lin et al., 2005a,b). In a recent review paper, Sturhahn & Jackson (2007) explained the basics of the NRS methods and summarized their geophysical applications in determining sound velocity, Grüneisen parameter, valence and spin state, and magnetic ordering of iron-bearing materials at high pressure.

An important application of the NRIXS technique is measuring the sound velocities of opaque samples under high pressure. From the NRIXS spectra, the partial phonon density of states (PDoS) of iron can be extracted. A parabolic fit to the PDoS at the low-energy region gives the Debye sound velocity V_D, which is related to the compressional wave velocity V_P and shear wave velocity V_S (Hu et al., 2003). X-ray diffraction (XRD) is a classical method for investigating the structures of crystalline solids. With brilliant and focused synchrotron X-ray sources, the XRD method has been widely used for equation-of-state (EoS) studies under high pressure. Combining V_D from NRIXS measurements and ρ and K_S from separate XRD experiments, the sound velocities of a number of iron-rich alloys have been derived (Mao et al., 2001, 2004; Lin et al., 2003a, 2004, 2005a; Gao et al., 2008).

Recently, a new experimental capability has been established at beamline 3-ID-B of the Advanced Photon Source (APS), Argonne National Laboratory (ANL), allowing for simultaneous XRD and NRS measurements of compressed samples in the panoramic DAC. In this paper, we describe the
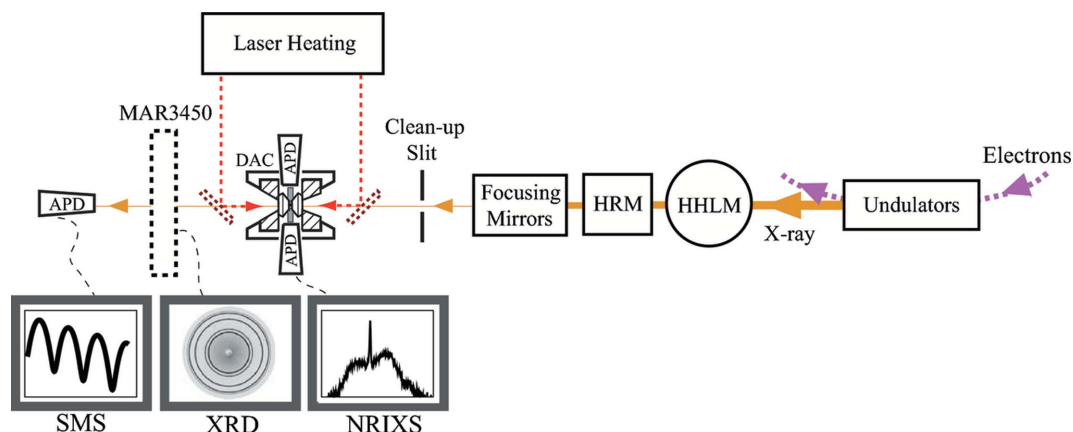
Figure 1
Experimental set-up at beamline 3-ID of the Advanced Photon Source at Argonne National Laboratory, showing the optics including high-heat-load monochromator (HHLM) and high-resolution monochromator (HRM), the instruments on the lower deck including those for nuclear resonant inelastic X-ray scattering (NRIXS), X-ray diffraction (XRD) and synchrotron Mössbauer spectroscopy (SMS), and the laser-heating system on the upper deck. The sample is mounted in a diamond anvil cell (DAC) for high-pressure experiments. Three avalanche photodiode (APD) detectors collect NRIXS signals within a plane that is perpendicular to the synchrotron radiation source, along the radial direction of the DAC. One APD detector records SMS signals in the forward direction, along the axial direction of the DAC. The MAR3450 image plate can be moved in for XRD measurements or out for SMS measurements.

new XRD set-up, focusing on the importance of simultaneous XRD and NRIXS measurements for determining sound velocities at high pressures and high temperatures.

2. Experiments

The experimental set-up at beamline 3-ID-B consists of integrated NRS and XRD instruments that are compatible with the laser-heated DAC technique (Fig. 1).

2.1. Nuclear resonant scattering

The NRS techniques include SMS and NRIXS. Mössbauer experiments in the time domain have been reported as early as the 1960s (Lynch *et al.*, 1960). More than 20 years later, the feasibility of Mössbauer experiments in the time domain using a synchrotron source was demonstrated (Gerdau *et al.*, 1985). In the 1990s, the first NRIXS experiments were conducted (*e.g.* Seto *et al.*, 1995; Sturhahn *et al.*, 1995). Both SMS and NRIXS require a photon source with a defined time structure and high flux. With the advent of the third-generation synchrotron sources, these types of experiments are readily achievable.

The NRIXS and SMS set-ups in our measurements are similar to those described by Sturhahn & Jackson (2007). The laser-heating set-up is described by Zhao *et al.* (2004) and Lin *et al.* (2005b). NRS experiments are carried out at the undulator beamline 3-ID-B during standard operating mode, with the 102 mA accelerator ring current evenly distributed over 24 electron bunches. The ring current is kept constant by a continuous 'top-up' at intervals of 2 min. The individual electron bunches are spaced 153 ns apart. Two undulators with a combined length of 4.8 m and a period of 27 mm are used. With a deflection parameter of $K = 0.65$, a photon beam at

14.41 keV can be generated at the first harmonic, providing a total flux of 10^{17} photons s^{-1} over a bandwidth of 500 eV.

NRS experiments require a small energy bandwidth in the incident X-ray beam (*e.g.* Sturhahn, 2004). This is achieved by two successive monochromators: a water-cooled high-heat-load monochromator (HHLM) and a high-resolution monochromator (HRM) (Toellner, 2000). The HHLM consists of two diamond (111) crystals of size $\sim$4.5 mm $\times$ 8 mm. From the incident beam, it selects photons of $\sim$14.41 keV with an energy bandwidth of $\sim$1.1 eV. The X-ray beam coming out of the HHLM has a flux of 1.5×10^{13} photons s^{-1} eV^{-1}. The HRM, composed of four silicon crystals, further reduces the bandwidth to 1 meV (Toellner *et al.*, 2006) and the X-ray flux to 4.5×10^9 photons s^{-1} over the 1 meV bandwidth.

The X-ray beam needs to be focused to match the small sample size in high-pressure experiments utilizing DACs. A bimorph mirror with 16 electrode elements focuses the beam in the horizontal direction (Signorato *et al.*, 1998). In the vertical direction, the beam is focused with an actively bent mirror in a Kirkpatrick–Baez arrangement (Eng *et al.*, 1998). The focused beam is $\sim$10 µm in both horizontal and vertical directions. To block unwanted background from small-angle scattering, a pair of clean-up slits are placed between the focusing mirrors and the sample.

The NRS scattering signals from the sample are collected using silicon avalanche photodiode (APD) detectors (*e.g.* Kishimoto, 1992; Toellner *et al.*, 1994; Baron & Ruby, 1994; Sturhahn, 2004). In NRIXS experiments, three APD detectors are placed around the sample in a plane that is perpendicular to the X-ray beam. They collect delayed photons produced in the nuclear decay process, including the directly emitted nuclear fluorescence photons at 14.4 keV and the $K\alpha$ fluorescence photons at 6.4 keV (*e.g.* Seto *et al.*, 1995). One APD detector is placed along the beam to collect photons at 14.4 keV in the forward direction. Each APD detector has an

area of 10 mm × 10 mm and a typical time resolution of ~1 ns (Sturhahn, 2004). The efficiency of the APD detectors is ~80% for the 6.4 keV photons and ~22% for the 14.4 keV photons. The efficiency can be improved by tilting the detector to increase the X-ray path inside the detector.

A statistically meaningful NRIXS spectrum requires hours to days of data collection. Generally, a number of one-hour NRIXS spectra are collected and added together. The count rate depends on the sample size and geometry. With the incident beam along the axial direction of the DAC, a thick sample with a small diameter gives the highest count rate. The count rate usually decreases upon compression as the sample becomes thinner and larger, resulting in a smaller sample volume exposed to the X-ray and stronger self-absorption of the NRIXS signals. At high temperature, the count rate increases owing to enhanced phonon excitation.

2.2. X-ray diffraction

Recently, an angular-dispersive XRD instrument was established and integrated with the NRIXS, SMS and laser-heating set-ups at beamline 3-ID-B (Fig. 1). A MAR3450 image plate, placed between the downstream mirror of the laser-heating system and the APD for SMS measurements, records the XRD signals. It can be moved into or out of the X-ray path using computer-controlled motors. In this study, the XRD data collection time ranges from 50 s at ambient conditions to 10 min at 17 GPa and ~1000 K.

For measurements on iron-bearing materials, the incident X-rays are tuned to 14.4125 keV ($\lambda = 0.86025$ Å). This low energy limits the accessible range of 2θ. For high-pressure studies, the accessible range of 2θ depends on the configuration of the DAC and the size and position of the image plate. Our DACs have an opening angle of 60°. We used two types of tungsten carbide (WC) seats, one with a 1.0 mm circular opening and therefore a 30° opening angle, and the other with a 2.3 mm-long slot opening and therefore a 60° maximum opening angle (Fig. 2). With a typical diamond thickness of 2.2 mm, these seats allow ~26° and ~55° access to the sample inside the cell. We consider these angles as the effective opening angles of the cells. The image plate is 345 mm in diameter and located ~320 mm away from the sample, covering a ~60° angular range when centered with the sample. It can be moved off-center to cover as much as 120° opening angle. The accessible range of 2θ is, therefore, not limited by the image plate. To maximize the 2θ range, we use the slot WC seat on the downstream side of the cell. With the X-ray beam aligned with the axial direction of the cell, the maximum allowed 2θ is half of the effective opening angle, i.e. 13° for the seat with 1.0 mm circular opening and 27.5° for the slot seat.

At 14.4125 keV, a maximum 2θ of 27.5° corresponds to a minimum d-spacing of 1.810 Å, according to Bragg's law, $2d \sin\theta = \lambda$. At ambient conditions, the major diffraction peaks of Fe$_3$C have d-spacings at 2.014 Å to 1.973 Å, and the major diffraction peak of NaCl has a d-spacing of 2.570 Å. With the current beam and cell configurations, we can observe most of the major peaks of Fe$_3$C and NaCl. As the d-spacing decreases
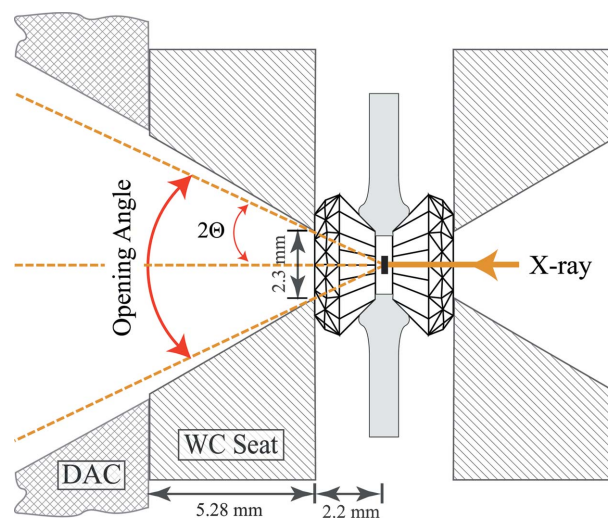

Figure 2
Schematic view of the DAC configuration, showing its effective opening angle and the range of 2θ accessible to the XRD measurements. See text for details.

with increasing pressure, however, the limited range of accessible d-spacing would hinder the use of the XRD set-up for measuring sample pressure, structure and lattice parameters.

To expand the accessible 2θ range, we could rotate the DAC so that the X-ray enters along the side of the seat opening, instead of through its center. This could potentially double the maximum 2θ if we use symmetrical DACs and slot seats on both sides of the cell. When panoramic DACs are used, the long cylinder would put a limit on the accessible 2θ range, and alternative ways are needed to increase the range. One option is to change the energy of the incident X-ray beam from the undulator source from 14.4125 keV (the first harmonic) to 43.2375 keV (the third harmonic). Increasing the X-ray energy to 43.2375 keV does not increase the maximum 2θ, but would reduce the minimum d-spacing to 0.621 Å. Replacing the WC seats with X-ray-transparent cubic boron nitride (cBN) seats would expand the accessible 2θ range and hence reduce the minimum d-spacing.

2.3. Sample preparation

A number of Fe$_3$C samples were synthesized from iron and graphite powders (Sigma-Aldrich, #282863) in an MgO capsule, using the piston-cylinder and multi-anvil large-volume presses at the University of Illinois. In synthesis runs 002 and 090, we used 94.45% ^{57}Fe-enriched iron powder from Cambridge Isotope Laboratories (#FLM-1812-0). In run 002, we followed the same procedure as described by Li et al. (2002). In run 090, a mixture with an atomic ratio of Fe:C = 2.922:1 was equilibrated at 3 GPa and 1373 K for 19 h. In synthesis run 093, we made fine powder of ^{57}Fe from a piece of ^{57}Fe foil at Argonne National Laboratory by dissolving the foil into hydrochloric acid and nitric acid to form hydroxide, then oxidizing it to Fe$_2$O$_3$, and eventually reducing it in H$_2$ gas to
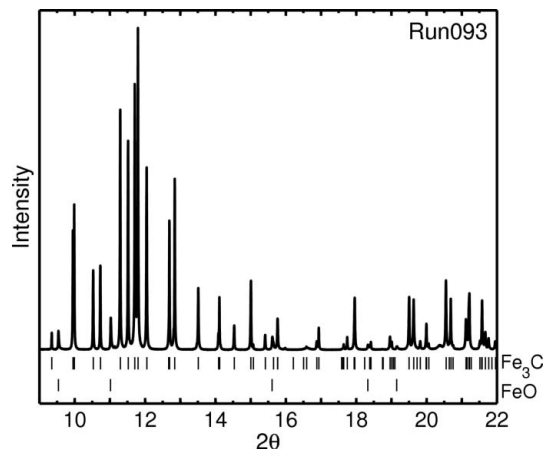
Figure 3
X-ray diffraction spectrum of Fe_3C from synthesis run 093 (λ = 0.41416 Å). Tick marks indicate the expected peak positions of Fe_3C and an impurity phase, which can be indexed as FeO with f.c.c. structure. The integrated intensity of the FeO peaks accounts for <3% of the total intensity.
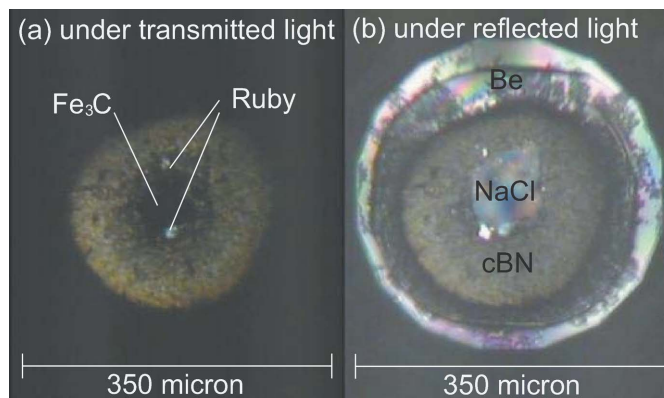

Figure 4
Typical sample configuration in the DAC. The Fe_3C sample is sandwiched between NaCl layers and surrounded by cBN, which is packed inside a beryllium gasket.

powder with an average grain size of <1 μm. A stoichiometric mixture was equilibrated at 2 GPa and 1373 K for 4 h.

To examine the purity of the synthesized Fe_3C, we measured their XRD patterns and conventional Mössbauer spectra (CMS) with a 5 mm × 5 mm-sized ^{57}Co γ-ray radioactive source at Sector 3 of the APS. The samples were ground into small grains with an average particle size of ∼2 μm. We mixed 0.16 mg of the sample with flour to reduce the effective thickness of ^{57}Fe to ∼3, equivalent to ∼0.3 μm of $^{57}Fe_3C$. The XRD data (Fig. 3) were collected at beamline 11-BM-B of the APS, using a monochromatic X-ray beam that is at least 100 μm in diameter (λ = 0.41416 Å).

Panoramic DACs with X-ray-transparent Be gaskets were used to generate high pressure. To minimize self-absorption of the NRIXS signals by the sample, the sample chamber was kept within a diameter of 70 μm. In some runs, a cBN insert, made from cBN powder (Alfa Aesar, 4–8 μm powder #40607) and epoxy (Versachem Clear Weld Epoxy System, #47609) at a ratio of 4:1 by weight, was used to reduce gasket shrinkage at high pressure (Lin *et al.*, 2003b). The Fe_3C sample was sandwiched between two NaCl layers. Ruby balls were placed next to the sample as pressure markers (Fig. 4).

2.4. NRIXS, SMS, CMS and XRD data evaluation

From the NRIXS spectra, the PDoS of Fe in Fe_3C was extracted using the program *PHOENIX* (Sturhahn, 2000). A series of one-hour NRIXS spectra collected under the same pressure and temperature conditions were added together, to obtain sufficient statistics. The Debye sound velocity (V_D) was derived from a parabolic fitting to the low-energy portion of the PDoS, between 3 and 12 meV, following the relation

$$\rho V_D^3 = \frac{\tilde{M}}{2\pi^2\hbar^3}\frac{g(E)}{E^2},\qquad(1)$$

where ρ is density, $g(E)$ is the PDoS, $\hbar$ is the reduced Plank's constant and $\tilde{M}$ is the atomic mass of ^{57}Fe (Hu *et al.*, 2003).

The *CONUSS* program (Sturhahn, 2000) was used to fit the SMS and CMS spectra, in order to obtain magnetic hyperfine parameters, the percentage of each phase and the sample thickness. The magnetic hyperfine parameters include the magnetic hyperfine field strength (HF), quadrupole splitting (QS) and the isomer shift (IS) between different phases if multiple phases are present.

The image-plate XRD data were analyzed using the *FIT2D* program. We used the *CMPR* program (Toby, 2005) for peak fitting, and calculated the lattice parameters using the weighted least-squares fitting method implemented in the program *UnitCell* (Holland & Redfern, 1997).

3. Results and discussion

3.1. Effect of impurity on sound velocity measurements

Our SMS measurements of the $^{57}Fe_3C$ from run 002 revealed iron impurity on the micrometer scale. The amount of excess iron varied from 0 to 90%, indicating inhomogeneous distribution of the iron impurity in the sample (Fig. 5, Table 1). The presence of such impurity appears to be related to the large grain size of the ^{57}Fe starting material, as pure Fe_3C was produced when natural iron with smaller grain size was used. If large grains of iron metal in the starting mixture were preferentially loaded into the sample capsule, the actual Fe:C ratio would be higher than that of stoichiometric Fe_3C.

The XRD spectrum collected at beamline 11-BM-B of the APS indicates that the product from synthesis run 093 is almost pure Fe_3C at the >100 μm scale (Fig. 3). The sextet in the Mössbauer spectrum also matches ferromagnetic Fe_3C with a hyperfine field of 20.4 (5) T, in accordance with the known value (Ron & Mathalone, 1971). Some individual pieces from run 093, however, were found to contain Fe or FeO impurity based on XRD measurements in the DAC. These pieces were discarded. In a high-temperature experiment, iron impurity was not detected at 300 K but appeared after being heated at 1400 K and 48 GPa for three days (Fig. 6). Excess iron might have been present as nanometer particles in the synthesized Fe_3C and grew into micrometer-size grains

Table 1
Magnetic hyperfine field parameters of Fe₃C and Fe.

Numbers in parentheses are uncertainties in the last digit(s), estimated from multiple fittings. HF, magnetic hyperfine field; QS, quadrupole splitting; IS, the isomer shift of Fe with respect to Fe₃C in the same loading. Run ID refers to the synthesis run number (002) and the loading information (AIR for a free-standing sample and DAC for a sample in a diamond anvil cell).

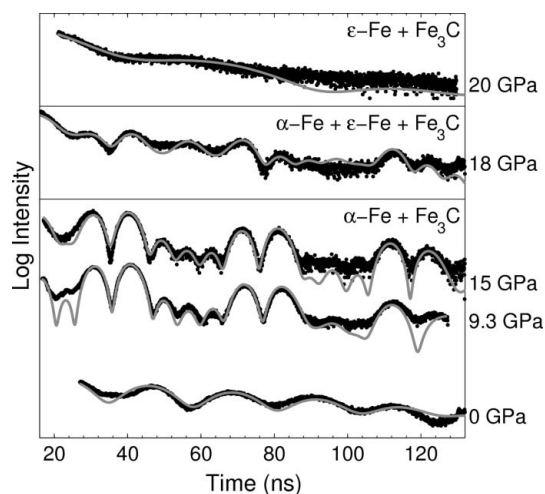| Run ID	P (GPa)	Fe₃C			Fe			
		HF (T)	%	QS (mm s⁻¹)	HF (T)	%	QS (mm s⁻¹)	IS (mm s⁻¹)
002-AIR-I	0	20.0 (5)	100	0.1 (1)	–	–	–	–
002-DAC-I	9.3 (1)	0 (1)	10 (3)	0.1 (2)	32.8 (3)	90 (5)	0.0 (1)	0.3 (1)
002-DAC-II	15 (1)	0 (1)	34 (5)	0.1 (2)	33.0 (3)	66 (5)	0.0 (1)	0.5 (1)
002-DAC-II	18 (1)	0 (1)	53 (5)	0.1 (2)	33.1 (1)	18 (5)	0.0 (1)	0.5 (1)
					1.5 (3)	29 (5)	1.2 (1)	0.5 (1)
002-DAC-III	20 (1)	0 (1)	64 (5)	0.2 (1)	1.5 (5)	36 (5)	1.2 (1)	0.3 (1)

Figure 5
Synchrotron Mössbauer data (black dots) and fit spectra (gray) of almost pure Fe₃C at ambient conditions and an Fe₃C sample containing iron impurity at high pressures (Table 1). The presence of iron is clearly indicated by the persistence of fast beats in the SMS spectra between 9.3 and 18 GPa, where Fe₃C is non-magnetic and b.c.c.-iron is magnetic. At 20 GPa, the b.c.c. (α) to h.c.p. (ε) transition and concurrent loss of magnetism in iron is complete, as indicated by the disappearance of fast beats in the SMS spectrum.
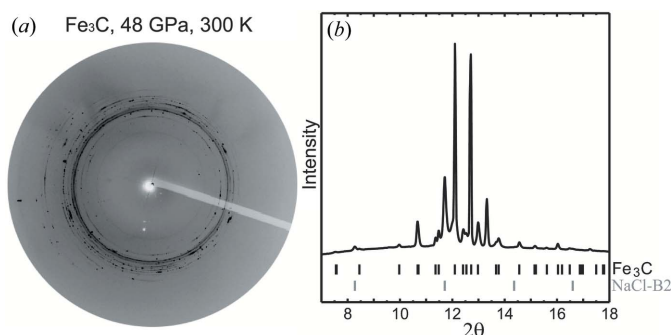

Figure 6
XRD data of a powder Fe₃C sample at 48 GPa and 300 K, after being heated at ~1400 K for about three days (run 090-DAC-III). The data were collected at beamline 16-ID-B of the APS (λ = 0.42348 Å). (*a*) Debye–Scherrer patterns recorded on the image plate. (*b*) The corresponding spectrum and expected peak positions of Fe₃C and NaCl. The peaks at 13.32° and 17.26° do not belong to Fe₃C or NaCl, but can be matched by h.c.p.-Fe.

upon heating. On the other hand, if excess carbon was present in the Fe₃C sample, it would react under high temperature to form Fe₇C₃ at pressures above 7 GPa (Bi *et al.*, 1993). *In situ* detection of iron impurity is therefore important for measuring the sound velocity of Fe₃C under high pressure and high temperature.

The presence of impurity may be detected on the basis of *in situ* XRD or SMS measurements. The SMS approach works if the impurity has a distinct magnetic property from the sample. At pressures below ~14 GPa, iron impurity in Fe₃C can be detected from the Mössbauer spectrum. At high pressures, however, this approach does not work because both iron and Fe₃C are non-magnetic and have similar hyperfine parameters. Compared with XRD, analyzing SMS data is much more time-consuming. The XRD approach is preferred as long as the relevant 2θ range can be accessed.

The effect of the iron impurity on the measured sound velocity of Fe₃C can be evaluated following Sturhahn &

Jackson (2007). Given that the Lamb–Mössbauer factors of iron and Fe₃C at 300 K are close to unity, the measured Debye sound velocity (V_D) of an Fe₃C sample containing an iron impurity with a concentration α can be approximated as

$$\frac{V_D}{V_{D,Fe_3C}} = \left\{ \frac{[(1-\alpha) + \alpha\xi][(1-\alpha) + \alpha\rho_{ratio}]}{(1-\alpha) + \alpha\xi\eta} \right\}^{1/3}, \quad (2)$$

where $\xi = f_{Fe}/f_{Fe_3C}$, $\eta = (\rho_{Fe}V^3_{D,Fe_3C})/(\rho_{Fe_3C}V^3_{D,Fe})$, $\rho_{ratio} = \rho_{Fe}/\rho_{Fe_3C}$, f is the Lamb–Mössbauer factor, ρ is the density, V_D is the measured Debye sound velocity and V_{D,Fe_3C} is the actual Debye sound velocity of Fe₃C.

The value of ρ_{ratio} is ~1.05 between b.c.c.-Fe and Fe₃C, and ~1.09 between h.c.p.-iron and Fe₃C. For conceivable V_{D,Fe_3C} that is 15% smaller or larger than that of the Fe (Mao *et al.*, 2001), η falls between ~0.6 and ~1.7. Assuming $\xi = 1$, which is reasonable for most iron-bearing materials under high pressure, 10% and 50% iron impurity would introduce an error of ~2% and ~9% in the measured Debye sound velocity, respectively (Fig. 7). The measured V_D is larger than the actual value for $\eta < 1$, and smaller for $\eta > 1$. These results suggest that a small amount of iron impurity (>10%) has a negligible effect on the measured Debye sound velocity of Fe₃C at 300 K. The
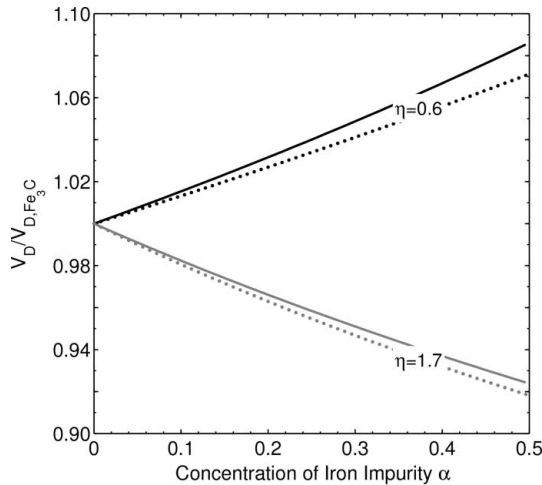
Figure 7
The effect of iron impurity on the measured Debye sound velocity of Fe_3C for a conceivable range of η between 0.6 and 1.7. The ratio between measured and actual Debye sound velocity $V_D/V_{D,Fe_3C}$ deviates from 1 as the concentration of iron impurity (α) increases. The density ratio between iron and Fe_3C (ρ_{ratio}) is ~ 1.05 for b.c.c.-iron (solid curves) and ~ 1.09 for h.c.p.-iron (dotted curves). The measured V_D is larger than the true value of V_{D,Fe_3C} for $\eta = 0.6$, and smaller for $\eta = 1.7$.
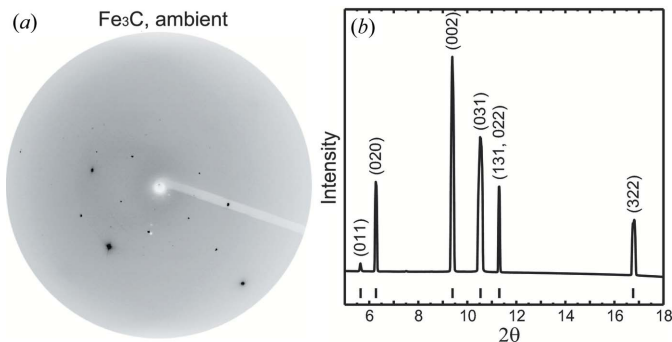

Figure 8
XRD data of a few-crystal Fe_3C sample in a panoramic DAC, under ambient conditions before compression (run 090-DAC-I). The data were collected at beamline 16-ID-B of the APS ($\lambda = 0.3694$ Å). (*a*) Spotty X-ray diffraction pattern recorded on the image plate. (*b*) The corresponding spectrum and expected peak positions (tick marks).

effect may be significant if the X-ray beam probes an iron-rich portion of the sample.

3.2. Sound velocities from simultaneous PDoS and EoS measurements

The XRD spectra collected at ambient conditions and 48 GPa reveal that at the micrometer scale our Fe_3C sample consists of a few single crystals in some runs and behaves like powder in others (Fig. 6, Fig. 8). We measured NRIXS spectra and derived the PDoS of a few-crystal Fe_3C sample between ambient conditions and 50 GPa at 300 K, and that of a powder Fe_3C sample at ambient conditions (Fig. 9).

Combining the PDoS and the existing EoS data (Scott *et al.*, 2001; Li *et al.*, 2002), we determined the compressional velocity V_P and shear wave velocity V_S (Fig. 10) using the following relations,
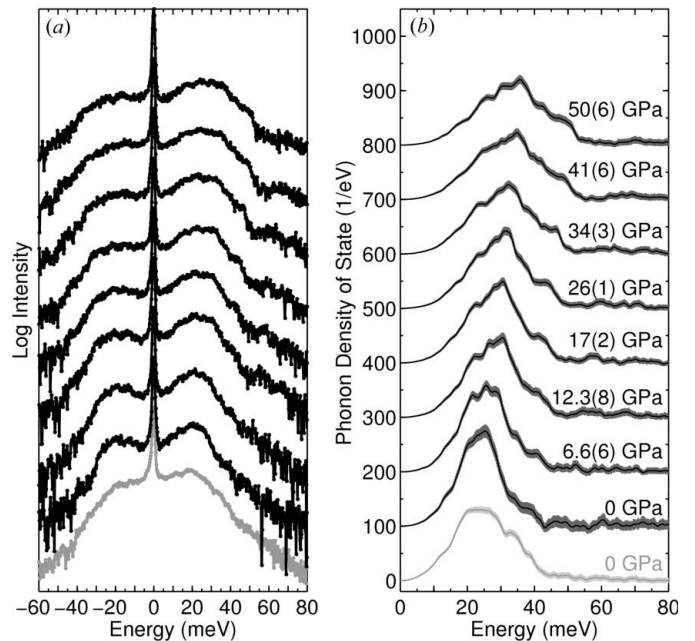

Figure 9
(*a*) NRIXS spectra of $^{57}Fe_3C$. (*b*) Corresponding partial phonon density of state (PDoS) of Fe in Fe_3C. Spectra at high pressures are vertically shifted for clarity. All spectra were collected on the few-crystal sample (Gao *et al.*, 2008) except for one measurement on a powder sample at ambient conditions (gray color).

$$\frac{3}{V_D^3} = \frac{1}{V_P^3} + \frac{2}{V_S^3}, \tag{3}$$

$$\frac{K_S}{\rho} = V_P^2 - \frac{4}{3} V_S^2, \tag{4}$$

where V_D is the Debye sound velocity extracted from the PDoS, density ρ and adiabatic bulk modulus K_S are EoS parameters. Our *in situ* XRD spectra (Fig. 11) provide a direct measure of the sample pressure and the unit cell volume, from which the density of Fe_3C can be calculated (Table 2). The measured density at ambient conditions (Table 2) differs from the known values by $\sim 0.2\%$–1%, corresponding to $\sim 0.1\%$–0.5% difference in V_P and V_S. At 48 GPa, our measured density differs from the existing EoS (Scott *et al.*, 2001) by $\sim 2.5\%$, corresponding to $\sim 1\%$ difference in V_P and V_S. The discrepancy between the measured and calculated density at high pressure and 300 K can be attributed to a pressure gradient in the sample inside the DAC. Indeed, the NaCl pressure (Birch, 1986) differs from the ruby pressure by ~ 4 GPa at 48 GPa (Table 2). An error in the measured sample pressure (dP) leads to an error in density according to d$\rho/\rho =$ dP/K. With a 10% error in pressure, the resultant error in density is $\sim 0.06\%$ at 1 GPa to $\sim 6\%$ at 100 GPa. With the approximation of $V_P \simeq 2V_S$ and ignoring dK/K, as K is less sensitive to errors in pressure, equation (4) implies that d$V_P/V_P \simeq$ d$V_S/V_S \simeq$ d$\rho/\rho/2$. A 10% error in pressure would therefore introduce a 0.03% error in the measured V_P and V_S at 1 GPa, and a 3% error at 100 GPa. The error is negligible at low pressure but significant at high pressure. The error can be

Table 2

Lattice parameters of NaCl and Fe₃C at high pressures.

P_{ruby}, pressure based on ruby R_1 fluorescence; P_{NaCl}, pressure based on EoS of NaCl. The unit cell volume of Fe₃C at ambient conditions and 300 K is 155.26 Å³ (Scott *et al.*, 2001) and 155.28 Å³ or 155.40 Å³ (Li *et al.*, 2002). The high temperature 750 K is estimated on the basis of detailed balance principle $I(E)/I(-E) = \exp(E/k_B T)$, where $I(E)/I(-E)$ is the probability ratio between phonon creation and annihilation, E is the nuclear resonant energy, k_B is Boltzmann's constant and T is the temperature. Numbers in parentheses are uncertainties in the last digit(s). The uncertainty in P_{ruby} is based on the pressure difference between different rubies and the pressure variation before and after the NRIXS measurements. Uncertainty in the lattice parameter is the error in least-square fitting of multiple peaks. Run ID refers to the synthesis run number (090 or 093) and the loading information (AIR for a free-standing sample and DAC for a sample in a DAC).

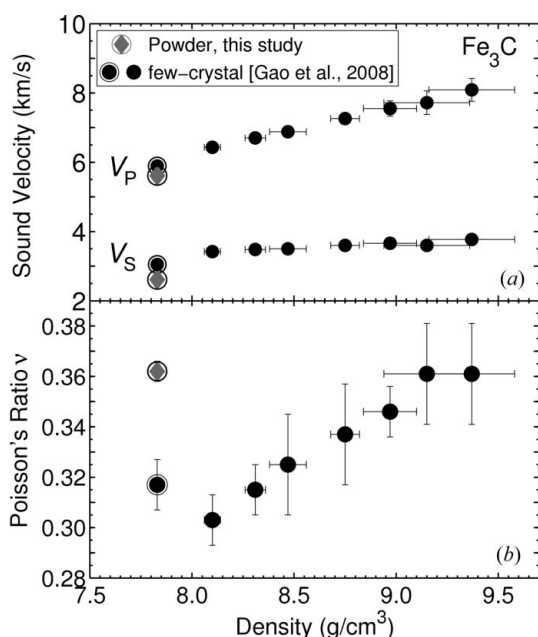| Run ID	P_{ruby} (GPa)	P_{NaCl} (GPa)	NaCl a (Å)	Fe₃C a (Å)	b (Å)	c (Å)	V (Å³)
300 K							
093-AIR-I	0	–	–	5.0813 (6)	6.7537 (8)	4.5139 (6)	154.90 (4)
090-DAC-I	0	–	–	5.158 (3)	6.748 (3)	4.510 (3)	157.0 (2)
090-DAC-II	17 (1)	16.9 (1)	5.065 (3)	4.969 (1)	6.574 (3)	4.4060 (7)	143.9 (1)
090-DAC-III	48 (3)	44.1 (1)	2.934 (1)	4.871 (1)	6.407 (3)	4.279 (1)	133.5 (1)
750 K							
090-DAC-II	–	15 (1)	6.139 (7)	5.018 (1)	6.587 (5)	4.4424 (8)	146.8 (2)

Figure 10
(a) Compressional wave velocity (V_P) and shear wave velocity (V_S) of Fe₃C at 300 K as a function of density, which is corrected for ⁵⁷Fe enrichment. At pressures below 6 GPa, Fe₃C is magnetic (marked by outer circles). At ambient conditions, the V_P and V_S of the few-crystal sample are 5% and 16% larger than those of the powder sample, respectively, indicating strong anisotropy. (b) Poisson's ratio ν of Fe₃C as a function of density. At ambient conditions, Poisson's ratio of the powder sample is larger and closer to the limiting value of 0.5 for liquids.

Figure 11
XRD spectra of Fe₃C at 17 GPa and 1000 K and 300 K (λ = 0.8603 Å). The small peak at ∼18° belongs to calcite, a minor contaminant which does not affect NRIXS measurements. The broad peak at 20.5° is the diffraction of the mirror in the laser-heating set-up.

eliminated through simultaneous PDoS and EoS measurements, which provide accurate sound velocities at a given density.

At high temperature, the presence of a temperature gradient could introduce additional errors in the measured velocities, if a separate EoS is used. The error in measured sample temperature (dT) leads to an error in density according to d$\rho/\rho = -\alpha\,dT$, where α is the thermal expansion coefficient. Assuming $\alpha = 10^{-5}$ K^{-1}, a temperature error of 200 K at 2000 K would introduce an error of 0.2% in ρ and therefore a negligible error of 0.1% in V_P and V_S.
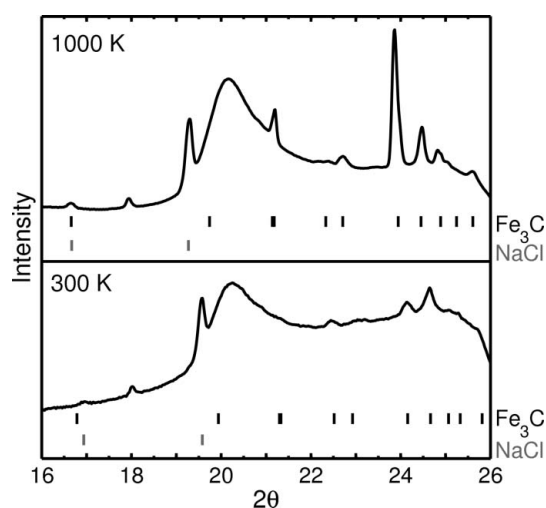
3.3. Grain size distribution and anisotropy

In NRIXS measurements, only the vibration modes projected in the direction of the incident X-ray beam contribute to the recorded signals. The PDoS spectrum of the sample, therefore, depends on the crystal orientation with respect to the incident X-ray beam (Chumakov *et al.*, 1997; Sturhahn & Kohn, 1999). Under ambient conditions, the NRIXS spectra and the corresponding PDoS of the few-crystal sample and powder sample are significantly different (Fig. 9). The derived V_P and V_S of the few-crystal Fe₃C are 5% and 16%, respectively, higher than those of the powder Fe₃C (Fig. 10).

Poisson's ratio ν is an elastic parameter defined as the strain in the direction normal to a uniaxial stress divided by the strain along the stress direction (Poirier, 2000). Poisson's ratio can be derived from V_P and V_S based on the following relationship,

$$v = \frac{3K_S - 2G}{2(3K_S + G)} = \frac{(V_P/V_S)^2 - 2}{2\left[(V_P/V_S)^2 - 1\right]}. \tag{5}$$

We found that Poisson's ratio of the powder sample is 14% larger than that of the few-crystal sample, and closer to the limiting value of 0.5 for liquids (Fig. 10). These results indicate that the sound velocity of Fe_3C is highly anisotropic, consistent with the recent report of extreme elastic anisotropy in cementite on the basis of first-principle calculations and XRD measurements (Nikolussi *et al.*, 2008). Using the elastic tensor of Nikolussi *et al.* (2008), we calculated the Debye sound velocity of Fe_3C in different orientations. Following Sturhahn & Kohn (1999), the directional dependence of V_D is well approximated by

$$\frac{1}{V_D^3} = \frac{1}{\bar{V}_D^3} - \frac{1}{V_{D,mod}^3} P_2[\cos(\theta)], \tag{6}$$

where $\bar{V}_D$ is the average of V_D, $V_{D,mod}$ is a term describing the modulation of V_D with the direction of the incident X-ray, θ is the angle between the *a* axis and the direction of the incident X-ray, and P_2 is the second-order Legendre polynomial, $P_2(x) = 0.5(3x^2 - 1)$.

We found that $\bar{V}_D = 3.245$ km s^{-1} and $V_{D,mod} = 4.07$ km s^{-1}. V_D is almost isotropic in the *bc* plane and more than 30% larger along the *a* axis. The maximum value of V_D is 4.11 km s^{-1} for X-rays incident along the *a* axis. Smaller values of V_D, as low as 3.02 km s^{-1}, are expected if the incident X-rays are perpendicular to the *a* axis. Our measured V_D of the few-crystal sample is ~5% larger than that of the powder sample, indicating that the few crystals are oriented with the average *a* axis neither parallel nor perpendicular but at an intermediate angle to the incident X-rays. Our experimental values of V_P and V_S for the powder sample extracted using equations (3) and (4) are both within 12% of the calculated Voigt–Reuss–Hill average. With further development, the on-line XRD may allow quantitative determination of anisotropy in sound velocities of compressed and heated samples.

4. Conclusions

A new X-ray diffraction set-up at beamline 3-ID-B of the Advanced Photon Source, Argonne National Laboratory, is fully integrated with existing nuclear resonant scattering and laser-heating instrumentation, enabling on-line measurements of sample pressure and lattice parameters, as well as detection of impurity, phase transition and chemical reaction at the micrometer scale. The low energy of the incident X-rays (14.4125 keV, corresponding to 0.86025 Å) in ^{57}Fe NRS experiments limits the accessible range of the 2θ angle, but a number of options are available to expand the range.

Iron impurity was found in the Fe_3C synthesized from ^{57}Fe-enriched powder. In some cases the impurity may be present at the nanometer scale at ambient conditions and grow into micrometer-sized grains upon heating. The effect of Fe impurity on Debye sound velocity of Fe_3C (V_{D,Fe_3C}) at 300 K is negligible if the concentration of the impurity is less than 10%.

The error introduced by Fe impurity could be as large as 9% if the X-ray probes the Fe-rich portion of the sample. *In situ* detection of the impurity is critical to ensure data quality.

Previous measurements of sound velocities have combined PDoS and EoS data from separate measurements. This approach is reliable if the sample pressure is measured accurately. Under pressures near or above megabar, the pressure gradient in the DAC could lead to a significant error in the measured velocities. *In situ* measurement of sample pressure and density is therefore necessary for obtaining accurate sound velocities at a given density.

Our simultaneous XRD and NRIXS measurements under ambient conditions reveal considerable differences in the compressional wave velocity, shear wave velocity and Poisson's ratio between few-crystal and powder Fe_3C samples, indicating strong anisotropy in its sound velocities. This finding demonstrates a unique application of the integrated techniques, for investigating anisotropy in sound velocities at high pressures and high temperatures.

References

Baron, A. Q. R. & Ruby, S. L. (1994). *Nucl. Instrum. Methods Phys. Res. A*, **350**, 595–626.

Bi, X. X., Ganguly, B., Huffman, G. P., Huggins, F. E., Endo, M. & Eklund, P. C. (1993). *J. Mater. Res.* **8**, 1666–1674.

Birch, F. (1986). *J. Geophys. Res.* **91**, 4949–4954.

Chumakov, A. I., Rüffer, R., Baron, A. Q. R., Grünsteudel, H., Grünsteudel, H. F. & Kohn, V. G. (1997). *Phys. Res. B*, **56**, 10758–10761.

Eng, P. J., Newville, M., Rivers, M. L. & Sutton, S. R. (1998). *Proc. SPIE*, **3449**, 145–156.

Gao, L., Chen, B., Wang, J., Alp, E. E., Zhao, J., Lerche, M., Sturhahn, W., Scott, H. P., Huang, F., Ding, Y., Sinogeikin, S. V., Lundstrom, C. C., Bass, J. D. & Li, J. (2008). *Geophys. Res. Lett.* **35**, L17306.

Gerdau, E., Rüffer, R., Winkler, H., Tolksdorf, W., Klages, C. P. & Hannon, J. P. (1985). *Phys. Rev. Lett.* **54**, 835.

Holland, T. J. B. & Redfern, S. A. T. (1997). *Mineral. Mag.* **61**, 65–77.

Hu, M. Y., Sturhahn, W., Toellner, T., Mannheim, P. D., Brown, D. E., Zhao, J. & Alp, E. E. (2003). *Phys. Rev. B*, **67**, 094304.

Kishimoto, S. (1992). *Rev. Sci. Instrum.* **63**, 824–827.

Li, J., Mao, H. K., Fei, Y., Gregoryanz, E., Eremets, M. & Zha, C. S. (2002). *Phys. Chem. Mineral.* **29**, 166–169.

Lin, J. F., Fei, Y., Sturhahn, W., Zhao, J., Mao, H. K. & Hemley, R. J. (2004). *Earth Planet. Sci. Lett.* **226**, 33–40.

Lin, J. F., Shu, J., Mao, H. K., Hemley, R. J. & Shen, G. (2003b). *Rev. Sci. Instrum.* **74**, 4732–4736.

Lin, J. F., Struzhkin, V. V., Sturhahn, W., Huang, E., Zhao, J., Hu, M. Y., Alp, E. E., Mao, H. K., Boctor, N. & Hemley, R. J. (2003a). *Geophys. Res. Lett.* **30**, 1–4.

Lin, J. F., Sturhahn, W., Zhao, J., Shen, G., Mao, H. K. & Hemley, R. J. (2005a). *Science*, **308**, 1892–1894.

Lin, J. F., Sturhahn, W., Zhao, J., Shen, G., Mao, H. K. & Hemley, R. J. (2005b). *Advances in High-Pressure Technology for Geophysical Applications*, pp. 397–411. Amsterdam: Elsevier.

Lynch, F. J., Holland, R. E. & Hamermesh, M. (1960). *Phys. Rev.* **120**, 513–520.

Mao, H. K. *et al.* (2001). *Science*, **292**, 914–916.

Mao, W. L., Sturhahn, W., Heinz, D. L., Mao, H. K., Shu, J. & Hemley, R. J. (2004). *Geophys. Res. Lett.* **31**, L15618.

Nikolussi, M., Shang, S. L., Gressmann, T., Leineweber, A., Mittemeijer, E. J., Wang, Y. & Liub, Z. K. (2008). *Scr. Metall.* **59**, 814–817.

Poirier, J.-P. (2000). *Introduction to the Physics of the Earth's Interior*, 2nd ed., pp. 36–41. Cambridge University Press.

Ron, M. & Mathalone, Z. (1971). *Phys. Rev. B*, **4**, 774–777.

Scott, H. P., Williams, Q. & Knittle, E. (2001). *Geophys. Res. Lett.* **28**, 1875–1878.

Seto, M., Yoda, Y., Kikuta, S., Zhang, S. W. & Ando, M. (1995). *Phys. Rev. Lett.* **74**, 3828–3831.

Shen, G., Sturhahn, W., Alp, E. E., Zhao, J., Tollenner, T. S., Prakapenka, V. B., Meng, Y. & Mao, H. (2004). *Phys. Chem. Miner.* **31**, 353–359.

Signorato, R., Hignette, O. & Goulon, J. (1998). *J. Synchrotron Rad.* **5**, 797–800.

Sturhahn, W. (2000). *Hyperfine Interact.* **125**, 149–172.

Sturhahn, W. (2004). *J. Phys. Condens. Matter*, **16**, 5497–5530.

Sturhahn, W. & Jackson, J. (2007). *Advances in High-Pressure Mineralogy, Geological Society of America Special Paper*, edited by E. Ohtani, Vol. 421, pp. 157–174.

Sturhahn, W. & Kohn, V. G. (1999). *Hyperfine Interact.* **123/124**, 367–399.

Sturhahn, W., Toellner, T. S., Alp, E. E., Zhang, X., Ando, M., Yoda, Y., Kikuta, S., Seto, M., Kimball, C. W. & Dabrowski, B. (1995). *Phys. Rev. Lett.* **74**, 3832–3835.

Toby, B. H. (2005). *J. Appl. Cryst.* **38**, 1040–1041.

Toellner, T. S. (2000). *Hyperfine Interact.* **125**, 3–28.

Toellner, T. S., Alatas, A., Said, A., Shu, D., Sturhahn, W. & Zhao, J. (2006). *J. Synchrotron Rad.* **13**, 211–215.

Toellner, T. S., Sturhahn, W., Alp, E. E., Montano, P. A. & Ramanathan, M. (1994). *Nucl. Instrum. Methods Phys. Res. A*, **350**, 595–600.

Zhao, J., Sturhahn, W., Lin, J. F., Shen, G., Alp, E. E. & Mao, H. K. (2004). *High Press. Res.* **24**, 447–457.